In situ neutron measurements and modelling of the intergranular strains in the near-β titanium alloy Ti-β21S

Viwanou Hounkpati, Sylvain Fréour, David Gloaguen, Vincent Legrand, Joe Kelleher, Winfried Kockelmann, Saurabh Kabra

In situ neutron measurements and modelling of the intergranular strains in the near-β titanium alloy Ti-β21S

Viwanou Hounkpati[a*], Sylvain Fréour[a], David Gloaguen[a], Vincent Legrand[a], Joe Kelleher[b], Winfried Kockelmann[b], Saurabh Kabra[b]

[a]Université de Nantes, Centrale Nantes, Institut de Recherche en Génie Civil et Mécanique (UMR CNRS 6183), Equipe Etat Mécanique et Microstructure des Matériaux, 58 rue Michel Ange, BP 420, 44606, Saint-Nazaire Cedex, France
[b]ISIS, STFC Rutherford Appleton Laboratory, Chilton Didcot, Oxfordshire, OX11 0QX, United Kingdom

The intergranular lattice strains in the near-β titanium alloy Ti-β21S have been measured in the longi-tudinal and transverse directions during tensile loading using neutron diffraction. The obtained results have been modelled and explained using a two-phase elasto-plastic self-consistent model. We first identified the best set of the main model parameters (single crystal elastic constants, critical resolved shear stresses) and investigated the influence of these parameters on the behaviour of both the poly-crystal and the diffracting volume. Good agreement between the experimental results and those predicted by the model was found for the macroscopic stress-strain dependencies and lattice strain developments of Ti-β21S.

1. Introduction

Aerospace industries are turning more and more towards near-β titanium alloys due to their high oxidation resistance among many other interesting properties that they exhibit [1,2], in order to benefit from their improved structural durability. Since β-titanium alloys keep their good properties only up to moderate temperatures [1], their limitations are their low resistance to hot hydraulic fluid, which is one of the very few corrosive media for titanium in the aerospace environment. In response to this weakness, a metastable β alloy Ti−15Mo−3Nb−3Al−0.2Si (Ti-β21S) has recently been developed to offer a high specific strength, a good cold formability and especially to improve oxidation resistance, which would in turn enhance temperature strength, creep resistance as well as thermal stability [2,3].

The study of the elasto-plastic behaviour of this kind of alloy is more complex than that of the pure α titanium, both experimentally and in terms of modelling. These alloys display two complex phases [4]; the micro- and mesoscopic properties of which as well as their incidence on the overall behaviour are misunderstood and thus poorly mastered. A significant number of scientific challenges remain unresolved regarding plasticity of these β-metastable titanium alloys. They show alpha and beta phases, respectively hexagonal and body-centred cubic crystallographic structures, with different volume ratio and grain morphology depending on the undergone thermal or thermomechanical treatments and on the nature and the quantity of alloying elements [4–7]. The deformation of hexagonal structure materials, like the alpha phase Ti-alloys, is complex due to the multiplicity of possible slip modes: prismatic, basal or pyramidal (48 possible systems, if the two directions of each slip mode are considered). Regarding the cubic phase, the deformation can be accommodated thanks to 96 slip systems on {110}, {112} and {123} planes [8–10]. Since slips activation order is disrupted due to interaction between phases, it is difficult to establish a clear hierarchy between deformation modes for each phase. Indeed, the results obtained on the single-phase Ti-alloys [11–14] cannot be directly applied to multiphase ones. In addition, there are very few studies related to the beta phase of Ti-alloys [7,8,15,16].

Residual stresses can occur through a variety of mechanisms including plastic deformations, temperature gradients or structural changes [17,18]. At grain scale, residual stresses arise as a

* Corresponding author.
E-mail address: v.hounkpati@gmail.com (V. Hounkpati).

consequence of the mechanical anisotropy of the crystals, influencing the material properties. Therefore, the control of the residual stress distribution within the material is mandatory for optimizing the behaviour and durability of structural parts. Many studies, accounting for a realistic description of the microstructure of the material through scales transition models, have been conducted to predict the micro-mechanical behaviour of titanium alloys during plastic deformation. *In-situ* diffraction experiments are often used to facilitate the choice of the best set of model parameters [8,9,12,14] and thus validate the models. In the present paper, experimental and theoretical investigations of intergranular strain evolution in Ti-β21S samples during plastic deformation are performed. Diffraction methods are helpful techniques to characterize the mechanical state of polycrystalline materials at the grain level. *In situ* time-of-flight (TOF) neutron diffraction was used to measure changes in the d-spacings of lattice planes during tensile loading experiments due to its ability to measure intergranular strains. Besides, predictive scales transition models provide a powerful numerical tool for interpreting the experimental data collected owing to diffraction methods and thus enabling to understand how intergranular strains are generated. These elastic strain fields are related to deformation mechanisms that dependent on the crystallographic structure. The experimental part was thus complemented by a two-phase Elasto-Plastic Self-Consistent (EPSC) model used to describe quantitatively the material parameters (single crystal elastic constants (SECs), critical resolved shear stresses (CRSSs) …). The purpose of this study is to combine experimental observations (tensile tests and neutron diffraction) with the predictions of the EPSC model in order to explain the plastic behaviour of Ti-β21S. In other words, this coupled approach will provide a better understanding and interpretation of experimental results. For example, this will enable us to identify the slip systems responsible of the plastic activity within each phase.

2. Experimental study and results

2.1. Ti-β21S titanium material

The investigated Ti-β21S titanium alloy used in this work was provided by Goodfellow Company (France) in a rolled plate form (200 mm × 100 mm × 0.5 mm). Its chemical composition, in weight %, is: Mo (15), Nb (3), Al (3), Si (0.2), with balance Ti. Due to this proportion of alloying elements, Ti-β21S is a quasi- β alloy. The material microstructure exhibits equiaxed β grains with a mean size between 25 and 30 μm. However, α precipitates are still visible along the β grains boundaries as usually observed in some β metastable titanium alloys [19,20]. In order to study the anisotropy induced by the machining of the plate and thus, the influence of the loading direction, samples were cut both along the rolling (RD) and transverse (TD) directions of the sheet, as shown on Fig. 1. These samples will be denoted in the following text "RD-sample" and "TD-sample", respectively.

2.2. Material analysis

2.2.1. Texture

Texture measurements were performed on the as-received material at the GEM beamline at the ISIS facility neutron spallation source, Rutherford Appleton Laboratory (Didcot, UK). Detailed information about the instrument, the measurement technique and the sample geometry used to determine the crystallographic texture can be found in Refs. [21,22]. Only the texture of the β-phase has been successfully measured. The volume fraction of the α-phase in the studied alloy is not high enough to permit measurement of the crystallographic texture of this phase. Fig. 2 displays the

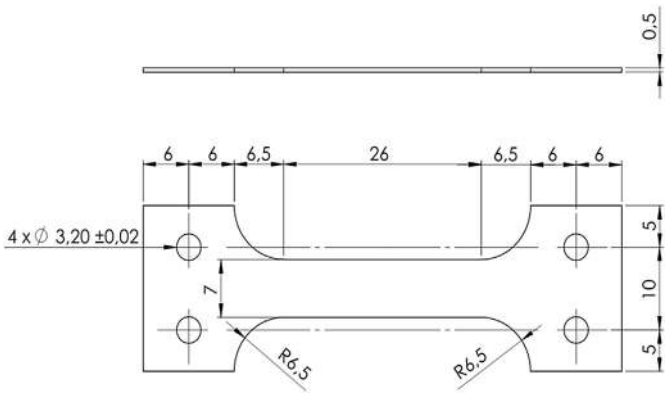

Fig. 1. Schematic view showing dimensions (in mm) of the samples used in diffraction experiments.

β {200} and {222} pole figures. These measurements show that the β-phase exhibits a weak texture: the highest intensity on the pole figures is actually only 2.04 multiples of a random distribution (mrd).

2.2.2. Volume fraction of the constituting phases

An X-ray technique based on the procedure developed by Averbach and Cohen [23] was used to determine the volume fraction of each phase. This procedure, more commonly known as the "direct comparison" method is applicable to randomly oriented or non-textured materials, where the integrated intensity from any diffraction peak is proportional to the volume fraction of the corresponding phase. Full information about this procedure can be found in Refs. [23–26]. One can note that for a textured sample, the intensity of a Bragg reflection does not only depend on the volume fraction of the diffracting phase, but also on its preferred crystallographic orientations. In this case, others methods can be used to correct the influence of texture on the quantitative phase analysis [24,25,27]. In order to determine the volume fraction of the phases constituting the studied samples, diffractograms were recorded from the as-received material on a four-circle XRD3003PTS Seifert goniometer using Cu Kα radiation. Several measurements were performed at different sample surface positions. The collected diffractograms present strong similarities in terms of peak intensity and 2θ-angle values, whatever the position on the surface of the specimen. This result confirms the homogeneity of the material. Fig. 3 shows one of these diffraction patterns. Due to the weak texture of the β-phase and the lack of texture knowledge for the α-phase, the actual volume fraction of each phase was determined by means of the classic direct comparison method of Averbach and Cohen [23]. The {11.0} and {20.1} peaks of the α-phase were less intense; thus, they were not exploited. As a consequence, the {10.0} and {10.1} reflecting lines were considered for this phase, instead. For the β-phase, {110}, {200} and {211} reflections were selected since their relative intensities are similar to those obtained in the case of analysis achieved on powder samples. According to the direct comparison method [23], the ratio between volume fraction of α and β phases is proportional to that between the intensities of α and β peaks. Indeed, for a lattice plane {*hkl*} of a given phase *i*, the integrated intensity I^i_{hkl} is proportional to the volume fraction f^i of this phase according to expression (1) below [23,25,27]:

$$I^i_{hkl} = KR^i_{hkl} f^i \quad (1)$$

where K is a constant factor connected with the measurement conditions (intensity and wavelength of the incident beam, mass

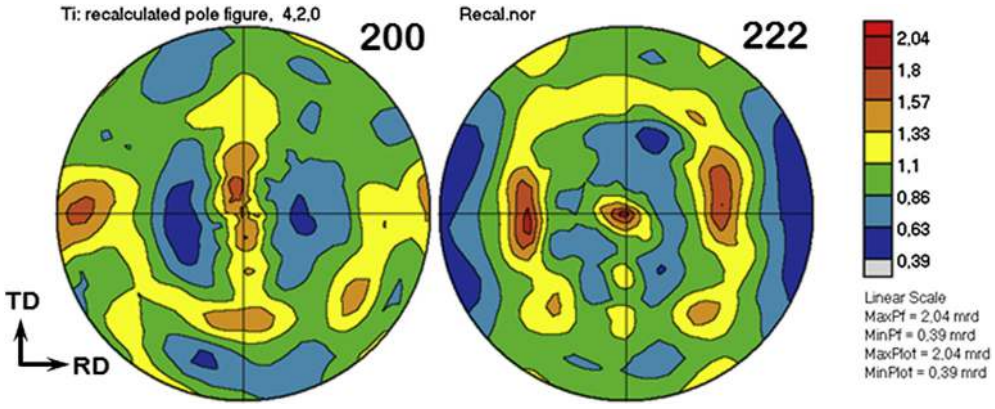

Fig. 2. β-phase texture pole figures of the as-received samples (RD: rolling direction, TD: transverse directions).

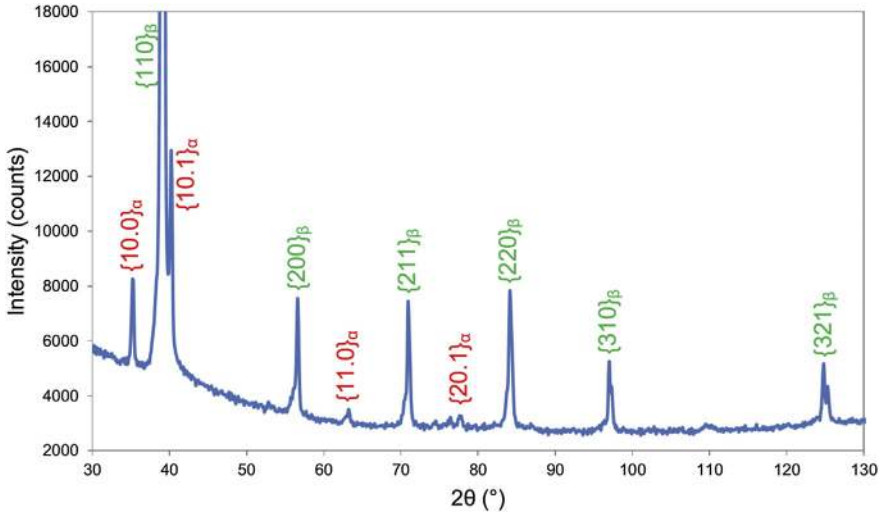

Fig. 3. Indexed diffraction pattern obtained with a four-circle XRD3003PTS Seifert goniometer using Cu Kα radiation, for the as-received material.

and charge of electron, diffractometer radius, …). Thus, K is independent of the investigated material. Besides, R^i_{hkl} is the reflectivity of the considered {hkl} lattice plane. Detailed expression of the reflectivity can be found in Refs. [23,25]. By writing the expression (1) of the integrated intensity for α and β phases (i = α, β) and by making the ratio of the two relations obtained, one can find:

$$f^{\beta} = \frac{I^{\beta}_{hkl}}{I^{\alpha}_{hk.l}} \frac{R^{\alpha}_{hk.l}}{R^{\beta}_{hkl}} f^{\alpha} \tag{2}$$

Knowing that $f^{\alpha} + f^{\beta} = 1$, the volume fraction of the α-phase can be expressed, for the chosen Bragg reflections, as:

$$f^{\alpha} = \left(1 + \frac{I^{\beta}_{hkl}}{I^{\alpha}_{hk.l}} \frac{R^{\alpha}_{hk.l}}{R^{\beta}_{hkl}}\right)^{-1} \tag{3}$$

This method was conducted to determine the volume fraction of the α-phase which was found equal to $f^{\alpha} = 10 \pm 1\%$. As a consequence, the volume fraction of the main β-phase is equal to the complement: $f^{\beta} = 90 \pm 1\%$.

2.2.3. Residual stresses

Some analyses have also been carried out using X-ray diffraction techniques to assess the residual stresses in the as-received samples. A χ-type goniometric assembly with Cu Kα radiation was used. The {321} plane family of the β-phase was studied at $2\theta = 125°$. Diffractograms were recorded for 16 tilt angles ψ varying between −48° and 45° and for two azimuthal angles: $\varphi = 0°$ and 90°. The direction $\varphi = 0°$ corresponds to the rolling direction. The set of diffraction peaks obtained for all the tilt angles were fitted simultaneously with a pseudo-Voigt function which takes into account the Kα1−Kα2 contribution. The centroid of the fitted diffraction line was taken as the peak position. For each diffraction peak, background was fitted through a polynomial function. The measurement ranges were chosen in order to cover an adequate number of points for a complete description of peak tails and background. The X-ray elastic constants ($S_1\{321\} = -3.2 \times 10^{-6}$ MPa^{-1}, ½ $S_2\{321\} = 13.7 \times 10^{-6}$ MPa^{-1}), needful for the stresses determination, were calculated with an elastic self-consistent model [18]. The normal residual stresses were 1 ± 19 MPa and −17 ± 24 MPa in the RD and TD directions, respectively. The corresponding shear residual stresses were −1 ± 4 MPa and 18 ± 5 MPa, respectively; values which are relatively low. The {321} peak integral widths were 0.463 ± 0.070° and 0.719 ± 0.155° in the RD and TD directions, respectively. These low values of integral widths show that our samples were initially weakly strain-hardened. According to all these results, residual stress removal was not mandatory prior to performing further investigations and they did not play a key role on the elastoplastic

behaviour. As a consequence, the samples were not annealed but were directly used for the *in situ* tensile tests described below.

2.3. In situ tensile tests and results

Neutron diffraction measurements were performed on the ENGIN-X beamline at the ISIS facility [28], using a 100 kN Instron universal testing machine. The ENGIN-X instrument presents a horizontal loading axis positioned at 45° to the incident beam. Two detector banks are set up horizontally and at angles ±90° to the incident beam, enabling simultaneous measurements of lattice strains from plane families lying parallel (loading direction, LD) and perpendicular (transverse direction, TD) to loading direction of the samples (Fig. 4). The Time-Of-Flight (TOF) technique enables collecting simultaneously an entire diffraction pattern (effective *d*-spacing range from 0.88 to 2.63 Å) by each detector, owing to the specificity of the neutron beam. The detector banks cover ±14° in the horizontal plane and ±21° in the vertical plane [28]. An extensometer was attached to the sample in order to make it possible to accurately measure the macroscopic strains experienced by the investigated specimen.

The specimens were subjected to a displacement controlled regime. A series of increasing uniaxial tensile loads was then applied as shown in Fig. 5. At each measurement point, a rapid stress relaxation (less than 50 MPa) was observed after loading of the specimen. For this reason, it is the measured points after relaxation which will be modelled, since this macroscopic mechanical state actually corresponds to that experienced by the material when the positions of the diffracting lines are gathered. The recording time was about 150 min for each measurement at a given macroscopic strain to obtain a good signal to noise ratio. Fig. 6 shows a typical measured diffraction pattern. Plane families {211}, {200} and {110} of the β-phase only were exploitable. The lack of α-phase reflections should be related to its low volume fraction, and correspondly, to low diffracted intensities. Non-indexed peaks observed in Fig. 6 at TOF = 37.5, 38.2 and 43 ms are parasite peaks induced by the crystalline sample holder material.

Single peak fitting was performed using the Open Genie code [29]. For each analysed peak, the elastic strain $\langle \varepsilon^{II}(\varphi,\psi,\mathrm{hkl})\rangle_{Vd}$ of a group of grains with a common {*hkl*} plane-normal parallel to the diffraction vector can be found from the measured lattice spacing $\langle \mathrm{d}(\varphi,\psi,hkl)\rangle_{Vd}$ and a reference lattice spacing $\mathrm{d}_0(hkl)$, using the following expression:

$$\left\langle \varepsilon^{II}(\varphi,\psi,\mathrm{hkl})\right\rangle_{Vd} = \frac{\langle \mathrm{d}(\varphi,\psi,hkl)\rangle_{Vd} - \mathrm{d}_0(hkl)}{\mathrm{d}_0(hkl)} \quad (4)$$

where ψ is the declination angle and φ denotes the rotation of the specimen around the specimen surface normal [18,30]. The reference point for this calculation is the initially measured $\mathrm{d}_0(hkl)$ for each lattice plane before deformation (prior to external mechanical loading) of the material. $\langle\rangle_{Vd}$ represents the volume average operation over the set of diffracting grains for the {*hkl*} reflection considered.

The lattice strains obtained were plotted as a function of the macroscopic strain (Fig. 7). Uncertainties calculated on the measured lattice strains are relatively low and vary from ±85 to ±485 micro-strains (10^{-6}). These results show the various behaviours in terms of deformation (due to the plastic anisotropy) of the principal families of grains {*hkl*}. According to the analysed plane family, crystallites groups have different crystallographic orientations. These crystallites activate different deformation modes, more or less intensively according to their orientation with respect to the loading axis. Initially, at the beginning of the loading, the material is in the elastic domain. There is therefore a linear variation of the measured lattice strains as a function of the applied macroscopic stress. Due to the elastic anisotropy, each crystallite group participating in the diffracting volume will present a behaviour more or less stiffer. For example, the stiffest plane families {211} and {110} show the lowest deformations in the elastic domain. On the contrary, the crystallite group corresponding to {200} which is less rigid, experiences more strains. Since the elastic behaviour is linear and especially due to the limited allocated beamtime, only three measurement points were chosen to characterize the elastic domain. More recording time was then spent to investigate the plastic domain, and specifically the elasto-plastic transition. The elasto-plastic transition is a second stage which is characterized by the deviation from linearity of the stress vs strain curve. This deviation indicates the onset of plastic deformation, well observed by a slight increase of lattice strains as a function of the applied load. An increase of elastic deformation therefore occurs in other grains which recover a part of the stress due to load transfer.

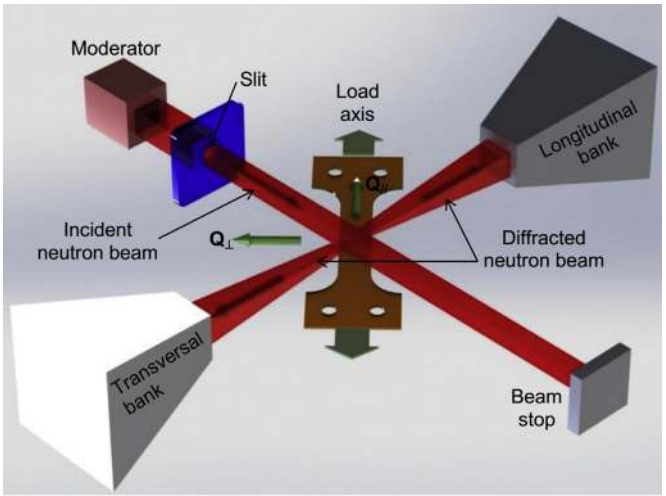

Fig. 4. Three-dimensional representation of the neutron diffraction instrument ENGIN-X (ISIS facility, UK). Strains are measured along the diffraction vectors $\mathbf{Q}_{//}$ and $\mathbf{Q}_{\perp}$. The volume of the sample explored by the instrument corresponds to the intersection of incident and diffracted beams.

3. Elastoplastic self-consistent modelling

EPSC models are a useful approach for modelling the mechanics of polycrystalline materials. The principles for using the self-consistent model to predict elastoplastic deformation were historically proposed by Kröner [31] and Hill [32]. In this context, each grain is considered as an ellipsoidal inclusion in a Homogeneous Effective Medium (HEM), whose properties are the average of all the other grains in the aggregate [33]. The polycrystal is represented by a weighted discrete distribution of orientations. A brief description is given below.

3.1. Single crystal plasticity

In the case of two-phase materials, single crystal plasticity of each phase is described in the same way as for single phase materials. In this work, the model developed in Refs. [34,35] is used and extended to two-phase materials. A detailed description of the EPSC model can be found in Refs. [36–38]. Owing to the study carried out in this work, the small strain formulation is sufficient because the macroscopic deformations are low (<10%). At such deformation levels, lattice rotation (reorientation by slip) and texture changes are limited. Therefore they will be neglected within the simulations.

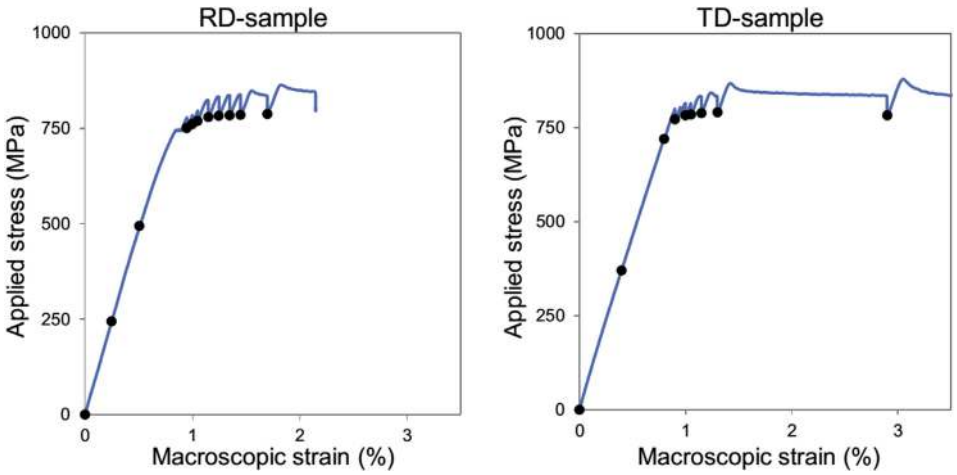

Fig. 5. Macroscopic stress–strain curves obtained during the diffraction experiment. The black dots represent the lattice strain measurement points.

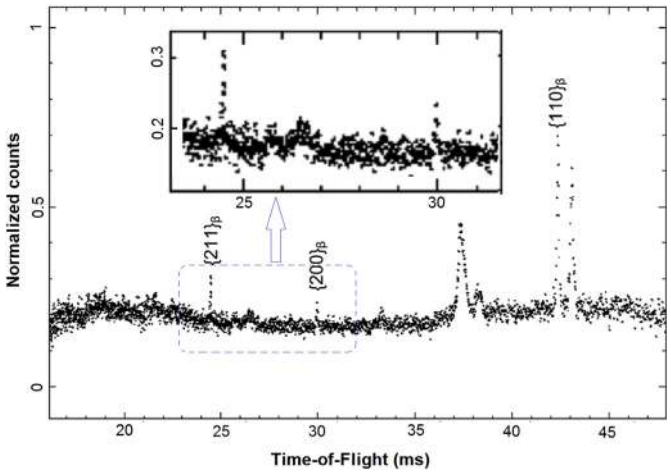

Fig. 6. Indexed diffraction spectrum obtained at ENGIN-X for the first lattice strain measurement point (prior to loading). Non-indexed peaks at TOF = 37.5, 38.2 and 43 ms are parasite peaks induced by the sample holder material.

The plastic flow can take place in a grain when the Schmid criterion is verified, i.e. slip (or twinning) occurs if the resolved shear stress τ^g on a system g is equal to the critical value τ_c^g depending on the hardening state of the slip system. This necessary condition is nevertheless insufficient. Thus, the complementary condition, which states that the increment of the resolved shear stress must be equal to the incremental rate of the CRSS, has to be checked simultaneously. The resolved shear stress is defined as the projection of the mesoscopic stress tensor σ^{II} on the considered deformation system. In small strain formulation, one has:

$$\tau^g = R^g : \sigma^{II} = \tau_c^g \text{ and } \dot{\tau}^g = R^g : \dot{\sigma}^{II} = \dot{\tau}_c^g \tag{5}$$

where R^g is the Schmid tensor on a system g. $A{:}B$ denotes the double scalar product $A_{ijkl}B_{klmn}$ using the Einstein summation convention.

The main issue to overcome is to determine which combination of deformation systems will actually be activated at each step of the plastic deformation path. Therefore, all possible combinations of potentially active systems should be scanned to find one that satisfies both the previous conditions (Eq. (5)) simultaneously. Because this must be done at each strain increment, running time considerations becomes one of the main technical issues of the

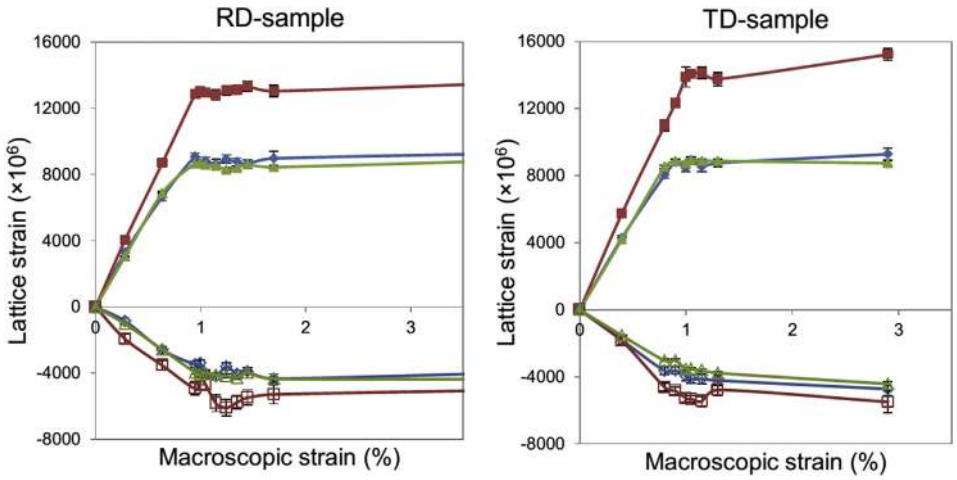

Fig. 7. Measured lattice strain for both RD- and TD samples in the loading direction (♦: {211}, ■: {200}, ▲: {110}) and transverse direction (◊: {211}, □: {200}, △: {110}) as a function of the macroscopic strain.

model. Moreover, this method can give several equivalent solutions for some hardening matrices [39]. In order to overcome these issues, Franz et al. [40,41] proposed a new formulation to determine the slip system activity in the elastoplastic regime. The accuracy of the simulations was also evaluated at the meso- and macroscopic levels by referring to mechanical experiments (tensile tests, neutron diffraction) [35]. It should be noticed that the "classic" EPSC model and the modified one provide similar results: the main active systems, predicted texture and residual strains are similar [42]. Based on Refs. [40,41], the slip rate $\dot{\gamma}^g$ on a system g can be expressed by:

$$\dot{\gamma}^g = K^g\left(\tau^g, \tau_c^g\right)\dot{\tau}^g \tag{6}$$

The slip rate is linked to the resolved shear stress rate $\dot{\tau}^g$ through a function K^g which is given by Refs. [40,41]:

$$K^g = \frac{1}{H^{gg}}\left(\frac{1}{2}(1+th(\tau^g))\right)\left(\frac{1}{2}\left(1+th\left(k\left(\frac{\tau^g}{\tau_c^g}-1\right)\right)\right)\right)\left(\frac{1}{2}(1+th(\dot{\tau}^g))\right)\dot{\tau}^g \tag{7}$$

where H^{gg} is the self-hardening parameter and k is a numerical parameter. The hyperbolic tangent (th) function [40,41] was tested and used because it enables the mechanical and hardening behaviours observed in practice to be reproduced.

The strain rate $\dot{\varepsilon}^{II}$ can be decomposed into its elastic ($\dot{\varepsilon}^{IIe}$) and plastic ($\dot{\varepsilon}^{IIp}$) parts:

$$\dot{\varepsilon}^{II} = \dot{\varepsilon}^{IIe} + \dot{\varepsilon}^{IIp} \tag{8}$$

The plastic strain rate $\dot{\varepsilon}^{IIp}$ is related to the tensor K^g and the slip rate $\dot{\gamma}^g$ of a system g by the expression

$$\dot{\varepsilon}^{IIp} = \sum_g R^g\dot{\gamma}^g \tag{9}$$

The slip rate of an active system g can be linked to the mesoscopic stress rate by the following equation:

$$\dot{\gamma}^g = K^g\dot{\tau}^g = K^gR^g : \dot{\sigma}^{II}(\text{without summation over g}) \tag{10}$$

Using the classical generalized Hooke's law and Eq. (10), the slip rate on a system g becomes:

$$\dot{\gamma}^g = K^gR^g : c : \dot{\varepsilon}^{IIe} \tag{11}$$

where c stands for the SECs (Single Crystal Elastic Constants) tensor. With Eqs. (8), (9) and (11), one obtains, after calculations, the following relation:

$$\dot{\gamma}^g = \sum_h\left(\delta_{gh} + K^gR^g : c : R^h\right)^{-1}K^hR^h : c : \dot{\varepsilon}^{II} \tag{12}$$

In Eq. (12), δ_{gh} is the Kronecker's delta.

A hardening matrix H^{gh} was introduced to describe the evolution of the CRSS rate in a system g, as a function of the plastic slip on the other systems:

$$\dot{\tau}_c^g = \sum_{h=1}^{n} H^{gh}\dot{\gamma}^h(\text{n being the number of active systems}) \tag{13}$$

3.2. Two-phase EPSC model

The single phase EPSC code [34,35] has been rewritten in Mathematica 8.0 software and adapted to two-phase polycrystalline materials. For a given phase i ($i = \alpha$ or β), the relation between the stress rate $\dot{\sigma}^{IIi}$ and the strain rate $\dot{\varepsilon}^{IIi}$ can be written for the mesoscopic scale as follows:

$$\dot{\sigma}^{IIi} = l^i : \dot{\varepsilon}^{IIi} \tag{14}$$

where l^i is the tensor of the elastoplastic tangent moduli of a single crystal of the phase i. Its expression can be found with relations (8), (12) and (13) and the classical generalized Hooke's law:

$$l^i(\mathbf{\Omega}) = c^i - \sum_g\sum_h c^i : R^g\left(\delta_{gh} + K^{gi}R^{gi} : c^i : R^{hi}\right)^{-1}K^{hi}R^{hi} : c^i \tag{15}$$

At the pseudo-macroscopic scale (phase's scale) and the macroscopic one, the corresponding relations between the stress rate ($\dot{\sigma}^{Ii}$ and $\dot{\sigma}^I$, respectively) and the strain rate ($\dot{\varepsilon}^{Ii}$ and$\dot{\varepsilon}^I$, respectively) are:

$$\dot{\sigma}^{Ii} = L^i : \dot{\varepsilon}^{Ii} \tag{16}$$

$$\dot{\sigma}^I = L : \dot{\varepsilon}^I \tag{17}$$

L^i and L are the tensors of the elastoplastic tangent moduli of the phase i and the polycrystal, respectively. The mesoscopic strain and stress rates of a single crystal of a phase i can be obtained through the localization A^i and concentration B^i tensors:

$$\dot{\varepsilon}^{IIi} = \left[S^{Esh} : L^{-1} : \left(l^i - L\right) + I\right]^{-1} : \dot{\varepsilon}^I = A^i : \dot{\varepsilon}^I \tag{18}$$

$$\dot{\sigma}^{IIi} = l^i : \left[S^{Esh} : L^{-1} : \left(l^i - L\right) + I\right]^{-1} : L^{-1} : \dot{\sigma}^I = B^i : \dot{\sigma}^I \tag{19}$$

where I is the fourth-order identity tensor, whereas S^{Esh} is the Eshelby tensor. The pseudo-macroscopic and macroscopic mechanical properties are obtained by the following volume averages over the mesoscopic properties:

$$\dot{\varepsilon}^{Ii} = \left\langle\dot{\varepsilon}^{IIi}\right\rangle_i,\ \dot{\sigma}^{Ii} = \left\langle\dot{\sigma}^{IIi}\right\rangle_i \tag{20}$$

$$\dot{\varepsilon}^I = \left\langle\dot{\varepsilon}^{IIi}\right\rangle_{\alpha,\beta},\ \dot{\sigma}^I = \left\langle\dot{\sigma}^{IIi}\right\rangle_{\alpha,\beta} \tag{21}$$

After some algebraic calculations, Eqs. (14), (18) and (20) give the pseudo-macroscopic elastoplastic tangent moduli tensor of the phase i:

$$L^i = \left\langle l^i : \left[S^{Esh} : L^{-1} : \left(l^i - L\right) + I\right]^{-1}\right\rangle_{\mathrm{i}} : \left\langle\left[S^{Esh} : L^{-1} : \left(l^i - L\right) + I\right]^{-1}\right\rangle_{\mathrm{i}}^{-1} \tag{22}$$

The overall elastoplastic tangent moduli tensor is given by:

$$L = \left\langle l^i : \left[S^{Esh} : L^{-1} : \left(l^i - L\right) + I\right]^{-1}\right\rangle_{\alpha,\beta} \tag{23}$$

Eq. (23) is a non-linear implicit equation, because the Eshelby tensor depends on the unknown L in the framework of EPSC theory. The Eshelby tensor S^{Esh} is calculated by an integral equation [37], which fully takes the plastic anisotropy into account. This Eq. (23) is

solved iteratively (as in the elastic case [30]) at each incremental loading step of the calculation.

4. Model parameters

The purpose of this study is to find a single set of material parameters to simultaneously describe the entire data set (i.e., the macroscopic stress–strain curve and the lattice strains measured on the various available reflections) in two principal directions and for the two kinds of samples (RD-sample and TD-sample). Table 1 summarizes the main parameters of the model. Accordingly, the volume fraction of each phase determined in the previous Section 2 was taken into account. Experimental pole figures of the β-phase were used to generate an orientation distribution function. A set of 1000 grain orientations weighted by the measured volume fraction has been selected from the experimental orientation distribution function (ODF) and used to model the texture of the β-phase. The α-phase was represented by a weighted discrete distribution (1000 grains) of random orientations (Euler angles (φ_1, ϕ, φ_2)). These numbers of grains are sufficient to describe correctly the experimental data (X-ray or neutron measurements) of two-phase titanium materials [8,9]. For the two phases each grain is considered as a spherical inclusion, as observed experimentally. The k value (Eq. (7)) is determined by comparison with a "classic" EPSC model under monotonic deformation (in terms of main active deformation systems and crystal reorientation). For all simulations, k is fixed to 25. The CRSSs are taken as identical for all equivalent systems of a system type. The deformation systems introduced in the model are assumed to be: basal slip (denoted B<a>), prismatic slip (P<a>), pyramidal slips (Π_1<a> and Π_1<c + a>). The second-order pyramidal slip Π_2<c + a> is not considered in our simulations. Indeed, this slip system was not (or rarely) experimentally observed as significantly active during the plastic deformation of two-phase titanium alloys [43,44]. Without assumption, there are 576 (= 24 × 24) elements in the H^{gh} matrix (Eq. (13)) for the α-phase and 2304 (= 48 × 48) for the β-phase, that need to be specified. To obtain a usable description of hardening, we opted for a more simplified form to keep a reasonable number of parameters. Thus, the following form is assumed for the hardening matrix [45]:

$$H^{gh} = qH^{hh} \tag{24}$$

Owing to a lack of relevant data on the nature of latent hardening in titanium alloys, the interactions between different deformation modes should be described by a simple law. The factor q determines the degree of latent hardening and is taken to be constant and fixed to a value of $q = 1.3$ for the simulations. In the present calculations, the constant value of H^{gg} (for a given deformation mode g) and q assumed for the plastic deformation lead to a linear hardening law. With these assumptions, apart from the factor q, only 4 parameters (H^{gg} values for the 4 deformation modes) are sufficient to describe the H^{gh} matrix for the α-phase and 3 others (H^{gg} values for the 3 deformation modes) for the β-phase.

In EPSC models, the most significant parameters are the SECs and CRSSs [8]. The experimental yield strength and curvature of the elastic–plastic transition at both diffracting volume and macroscopic scales were used as the fitting criteria to determine the best set of CRSS and self-hardening values for each phase. The final values that give the optimum agreement between the measured and predicted results were summed up in Table 2.

The SECs used for the α-phase in this model are: $c_{11} = c_{22} =$ 168 GPa, $c_{12} = 94.5$ GPa, $c_{13} = 69.3$ GPa, $c_{33} = 190.5$ GPa and $c_{44} =$ 48.8 GPa [46]. While there is agreement in the literature [8,14,46,47] for the SECs of the α-phase, the Ti-β SECs often strongly vary from one reference to another. The wide values of the SECs of the β-phase existing in the literature may be related to the nature and proportions of alloying elements that are present in this phase: both actually vary a lot from one alloy to another, contrary to the case of the α-phase. Table 3 summarizes some SECs of titanium β-phase published in the literature [8,19,48–50]. Figs. 8 and 9 show, for the RD-sample, the influence of these values on the macroscopic stress–strain curves and the lattice strain evolution of the β analysed plane families in the loading direction, respectively. Large changes of the macroscopic behaviour (especially during the elastic regime) depending on the choice of β SECs were observed. Indeed, due to the high volume fraction of the β-phase, the choice of its

Table 1
The main parameters of the model.

Parameters	α-phase	β-phase
Volume fraction	10%	90%
Number of grains	1000	1000
Grains morphology	equiaxed	equiaxed
Crystallographic texture	isotropic	experimental
SECs	*to be determined*	*to be determined*
CRSS	*to be determined*	*to be determined*
Hardening parameters	*to be determined*	*to be determined*

Table 2
CRSSs (τ_c) and self-hardening (H^{gg}) values used in the simulations.

Phases	Slip system	τ_c(MPa)	H^{gg}(MPa)
α-phase	B<a>	250	110
	P<a>	220	100
	Π_1<a>	350	170
	Π_1<c + a>	400	180
β-phase	{110}<111>	310	160
	{112}<111>	330	170
	{123}<111>	350	180

Table 3
Some literature single-crystal elastic constants (SECs) in GPa for the β-phase of titanium.

Materials	Label	c_{11}	c_{12}	c_{44}	Refs
Ti-17	β_SECs_FRE05	174.0	116.0	41.0	[48]
Ti-β	β_SECs_LED04	99.7	82.7	37.5	[49]
Ti-β	β_SECs_PET91	134.0	110.0	36.0	[50]
Ti-β21S	β_SECs_HER11	153.0	101.0	57.0	[19]
Ti-10-2-3 (forged)	β_SECs_RAG07F	140.0	128.0	50.0	[8]
Ti-10-2-3 (forged and aged)	β_SECs_RAG07A	165.0	118.0	45.0	[8]

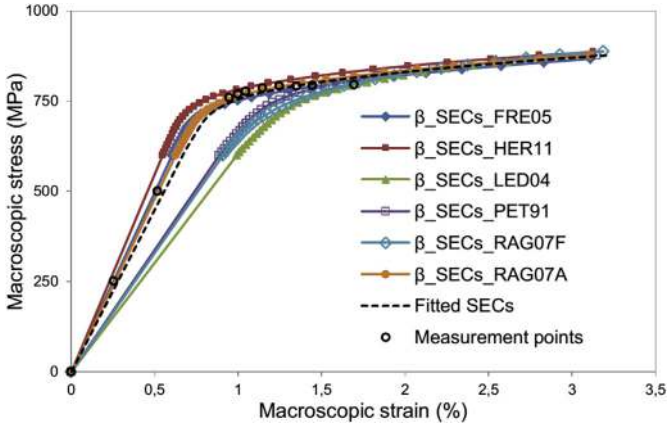

Fig. 8. Influence of the β SECs on the macroscopic stress–strain curves of the RD-sample.

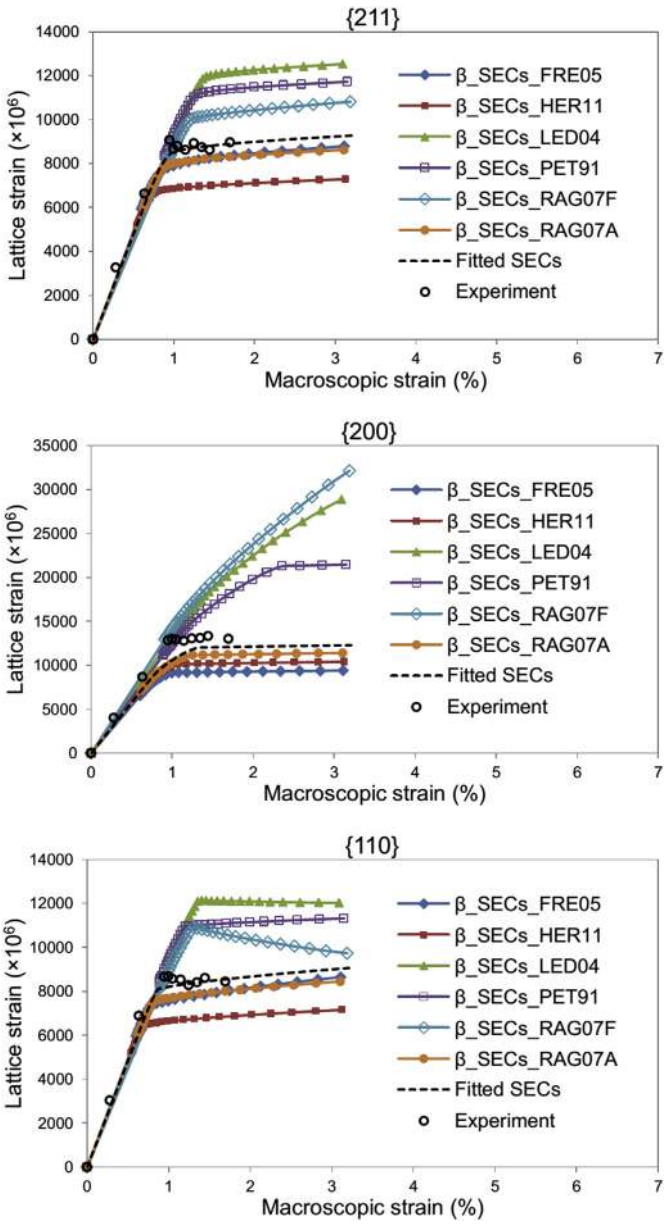

Fig. 9. Influence of the β SECs on the lattice strain of the β analysed planes family along the loading direction of the RD-sample.

SECs significantly affects the macroscopic (elastic) behaviour of this alloy. The Young's modulus varies from 60.6 GPa for SECs_LED04 values to 109.7 GPa for SECs_HER11 (see Table 3 for correspondence between labels, bibliographic references and SECs values). Only the single-crystal elastic constants SECs_FRE05 and SECs_RAG07A satisfactorily reproduce the measured macroscopic stress-strain curve. For example, at the macroscopic total strain of 1.4%, the relative deviations upon the applied stress are only −0.5 and 0.7% for SECs_FRE05 and SECs_RAG07A, respectively. However, the lattice strain curves obtained by these latter deviate significantly from the experimental values. For the same point (1.4% of macroscopic strain) for example, the relative deviations upon the lattice strain of the {200} family planes are −30.8 and 16.2% for SECs_FRE05 and SECs_RAG07A, respectively. Indeed, all these SECs (Table 3) do not simultaneously reproduce the meso- and macroscopic properties. For these reasons, the β-phase SECs were treated as additional fitting parameters and adjusted until a reasonably good agreement with the experimental data was reached at the diffracting volume and macroscopic scales. The final β SECs values fitted to the macroscopic and lattice strain behaviours in the models were: $c_{11} = 153.5$ GPa, $c_{12} = 109.7$ GPa and $c_{44} = 41.9$ GPa. These values are within the range of the data found in the literature for the β-phase of various titanium alloys. The macroscopic and lattice strain curves obtained for these values are shown on Figs. 8 and 9, respectively. One can notice an improvement compared to the curves obtained with the other SECs values (Table 3).

5. Results and discussions

Once all the model parameters were determined, the comparison between the results of our simulations and their experimental counterparts was carried out for the RD-sample and TD-sample at the macroscopic and diffracting volume scales. The results will be presented and discussed in this section.

5.1. Model comparison with the experimental macroscopic response

Fig. 10 shows the comparison between the measured and predicted stress−strain curves for RD-sample and TD-sample. The predicted and measured plastic slopes are identical up to 2% total strain. The Young's modulus calculated for the two kinds of sample are identical (89.9 GPa). This is due to the fact that equiaxed grains were considered in the simulation along with an almost isotropic crystallographic texture. The calculated Young's moduli are close to the experimental ones (96.8 GPa for the RD-sample and 91.1 GPa for the TD-sample). The model predictions for the macroscopic response of Ti-β21S are in good agreement with the experiment.

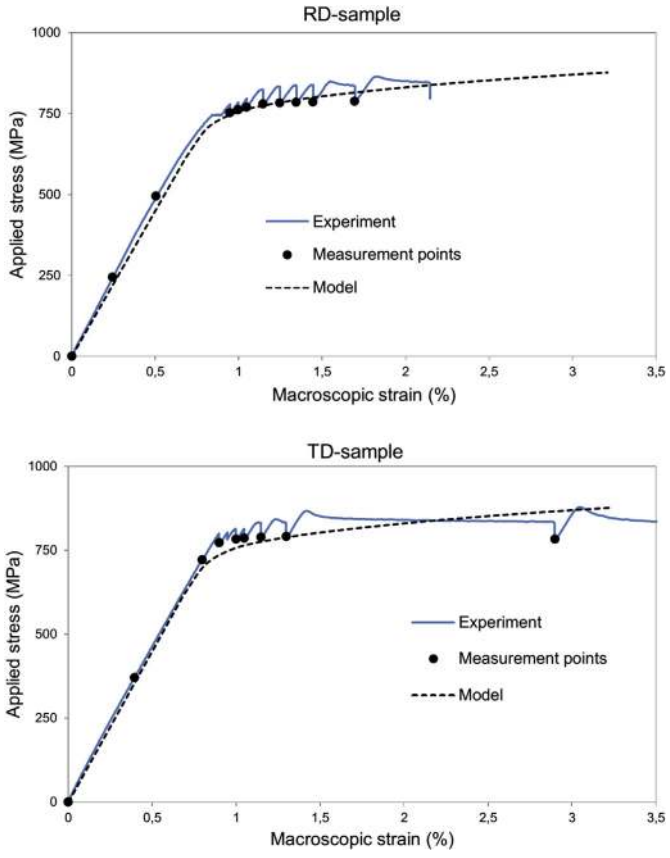

Fig. 10. Comparison between modelled and measured macroscopic stress−strain curves. Dots indicate neutron measurement points which are modelled in this study.

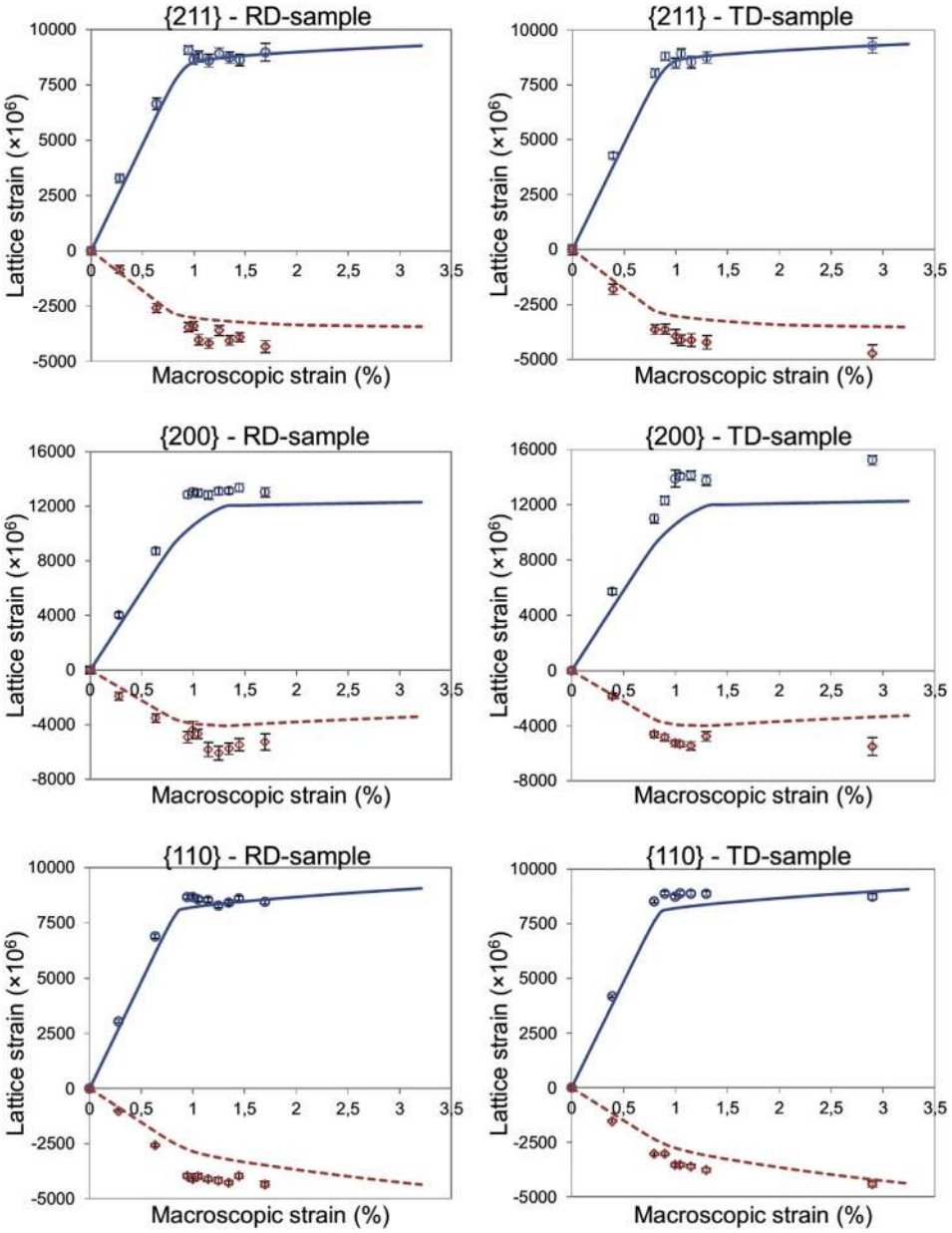

Fig. 11. Longitudinal (○: experiment, ▬: model) and transverse (◊: experiment, ▬: model) lattice strains vs. macroscopic strain for the β {hkl} plane families analysed.

5.2. Model comparison with the experimental lattice response

The development of the elastic strains in different grain orientations can be used as a useful and sensitive sensor of plasticity. Fig. 11 shows the longitudinal and transverse lattice strains vs. macroscopic strain for the β {*hkl*} reflections. At the mesoscopic scale, lattice responses are also similar for the two samples for the same reasons as discussed previously for the macroscopic response. However, different elastic and plastic responses were observed for each investigated grain family. Indeed, when a polycrystalline aggregate is submitted to a uniaxial loading in the elastic region, the lattice strains develop linearly with load up to the point of micro yielding. Owing to their inherent elastic anisotropy and their range of possible crystallographic orientations, there is a significant difference in the elastic response for each grain family (i.e., all grains with a particular {*hkl*} plane perpendicular to the scattering vector Q for the given detector bank). When plastic deformation occurs, slip activity is initiated in certain grains similarly orientated. The imposed deformation is plastically accommodated, and these grains carry less load.

A good agreement is reached between experimental data and model predictions in the longitudinal direction, except for the {200} family planes for which the lattice strains are underestimated by the model (with a maximum relative deviation of 20.3% at 0.9% total strain for the RD-sample and 24.4% at 1% total strain for the TD-sample). This deviation observed for the {200} family planes could be due to the morphological texture effects. Indeed, in our simulations, all crystallites (coherent diffraction domains) are assumed to be spherical. The form of some crystallites may be different from the equiaxed grain shape considered. This family of planes is very influenced by the morphological texture [30], this could explain these discrepancies. The low multiplicity of this plan (and therefore less grains in diffraction position) and the simplified description of the hardening may also explain these

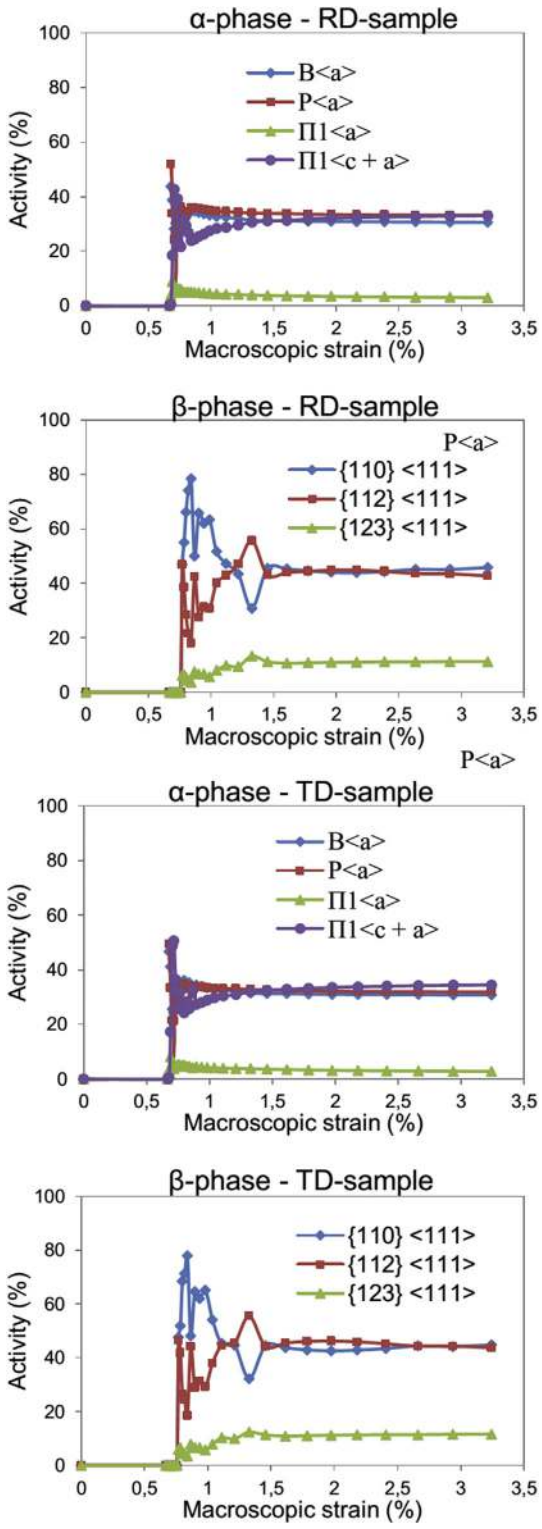

Fig. 12. Calculated relative contribution of each deformation mode of α- and β-phase to the total shear, as a function of macroscopic strain.

differences. Some authors encountered the same difficulties in the literature to simulate the behaviour of the diffracting volume for this plane. This is the case for example of Ti−10V−2Fe−3Al alloy where Raghunathan et co-workers [8] obtained very significant difference between the simulated lattice strain and the corresponding values measured on synchrotron for {200}.

One can notice that the discrepancies between model calculations and measurements are globally more pronounced perpendicularly to the tensile axis than in the longitudinal direction. Many authors pointed out this problem [51–54]. Indeed, all grains with a plane normal vector positioned along the transverse scattering vector, for a given {*hkl*} reflection, have a common (*hkl*) plane normal perpendicular to the loading axis. The grains which participate in the reflection have widely varying crystallographic orientations with respect to the loading axis. A grain rotation around an axis perpendicular to the loading direction highly changes the stiffness in the tensile direction and, thus, the strain and stress state in the grain. For the considered {*hkl*} reflection, the lattice strain of the diffracting grains shows wide variation. In the longitudinal direction, grains which contribute to a given {*hkl*} reflection are all oriented more-or-less identically relative to the loading axis: all the grains have the identical lattice plane normal in a direction parallel to the tensile axis. The lattice strains variation for all grains in the diffracting volume along the longitudinal direction is lower than that along the transverse direction within a given {*hkl*} family. Consequently, the predicted transverse strains are sensitive to small variations in the crystallographic texture representation, unlike the longitudinal direction.

The model predicts the yielding of {211}, {200} and {110} β-grains at 679 MPa (0.77% total strain) induced by the activation of the 3 slip systems of this phase. For the RD-sample, the corresponding lattice strains for the 3 β-grains families in the longitudinal direction are 7339, 8833 and 7382 micro-strain (units of 10^{-6}) respectively. In the transverse direction, the lattice strains corresponding to the β-grains yielding points are −2747, −3398 and −2346 micro-strains (10^{-6}) respectively. For the TD-sample, slight discrepancies are observed for the lattice strains corresponding to the β-grains yielding points: 7363, 8831 and 7379 micro-strains (10^{-6}) respectively in the longitudinal direction and −2720, −3399 and −2280 micro-strains (10^{-6}) respectively in the transverse direction.

Fig. 12 shows the relative contribution of each deformation mode of α- and β-phase to the total shear as a function of macroscopic deformation. The plastic activity is the same for the RD- and TD-sample because of the crystallographic texture almost isotropic. The plastic activity begins in the α-phase at 610 MPa (0.68% total strain) with 51.8% P<a>, 43.7% B<a>, 4% Π_1<a> and 0.5% Π_1<c + a>. In the β-phase, the plastic activity begins at 679 MPa (0.77% total strain) with 46.8% {110}<111>, 47% {112}<111> and 6.2% {123}<111>. With the CRSS values chosen (see Table 2), deformation is accommodated through B<a>, P<a>, Π_1<c + a>, {110}<111> and {112}<111>. As it can be seen in Fig. 12, the relative contributions of Π_1<a> and {123}<111> are small, as observed by Stapleton et al. [9]. In this work, the results obtained for specimens cut in both directions (longitudinal and transverse) of the plate are substantially similar. This is due, as mentioned above, to the crystallographic texture almost isotropic and the equiaxed grain shape. However, the model manages to capture these small differences at the macroscopic and diffracting volume scales.

6. Conclusion

A complete study concerning the development and the evolution of internal strains under mechanical loading in a metastable β alloy Ti−15Mo−3Nb−3Al−0.2Si (Ti-β21S) was made. Neutron diffraction techniques in combination with a modified two-phase EPSC model were used to interpret the lattice strain development and to deduce the main active deformation modes during uniaxial tensile tests. This capacity to measure intergranular strains provides a relevant experimental tool for understanding how intergranular strains are generated. Moreover, diffraction data offer a

rigorous test for the models at meso- and macroscopic levels.

The results from the model agree well with the macroscopic stress-strain curve and there is reasonable agreement with the longitudinal and transverse lattice strains evolutions of the β-phase. This indicates that combinations of different material parameters (SECs, CRSSs, hardening matrix …) determined in this work are suitable for this alloy. Due to the wide values of the SECs of the β-phase existing in the literature, their influence on the macroscopic stress−strain curves and the lattice strain evolution has been investigated in this work. The results show a strong influence of the SECs on plasticity, both on the macroscopic behaviour and at the diffracting volume scale.

Acknowledgements

The authors thank the ISIS neutron facility scientific committee for the allocated experimental days on ENGIN-X and GEM instruments (experiment RB1320149, ISIS, UK).

References

[1] R.R. Boyer, An overview on the use of titanium in the aerospace industry, Mater. Sci. Eng. A 213 (1996) 103−114.
[2] G. Welsch, R.R. Boyer, E.W. Collings, Materials Properties Handbook: Titanium Alloys, Materials, USA, 1994.
[3] P.J. Bania, W.M. Paris, Beta-21s: a high temperature metastable beta titanium alloy, Proc. Tech. Progr. from 1990 Int. Conf. Titan. 1990 Prod. Appl. 2 (1990) 784−793.
[4] K.G. Honnell, N. Velisavljevic, C.D. Adams, P.A. Rigg, G.N. Chesnut, R.M. Aikin, et al., Equation of state for Ti-beta-21S, in: AIP Conf. Proc, 2007, pp. 55−58, http://dx.doi.org/10.1063/1.2833146.
[5] B. Cherukuri, R. Srinivasan, S. Tamirisakandala, D.B. Miracle, The influence of trace boron addition on grain growth kinetics of the beta phase in the beta titanium alloy Ti−5Mo−2. 6Nb−3Al−0. 2Si, Scr. Mater. 60 (2009) 496−499, http://dx.doi.org/10.1016/j.scriptamat.2008.11.040.
[6] E. Aeby-gautier, B. Denand, J. Teixeira, M. Dehmas, B. Appolaire, A. Settefrati, Influence of microstructure on tensile properties of beta-metastable Ti 17 alloy, in: 12th World Conf. Titan., Beijing, 2011.
[7] A. Settefrati, E. Aeby-Gautier, M. Dehmas, G. Geandier, B. Appolaire, S. Audion, et al., Precipitation in a near beta titanium alloy on ageing: influence of heating rate and chemical composition of the beta-metastable phase, Solid State Phenom. 172−174 (2011) 760−765, http://dx.doi.org/10.4028/www.scientific.net/SSP.172-174.760.
[8] S.L. Raghunathan, A.M. Stapleton, R.J. Dashwood, M. Jackson, D. Dye, Micromechanics of Ti−10V−2Fe−3Al: in situ synchrotron characterisation and modelling, Acta Mater. 55 (2007) 6861−6872, http://dx.doi.org/10.1016/j.actamat.2007.08.049.
[9] A.M. Stapleton, S.L. Raghunathan, I. Bantounas, H.J. Stone, T.C. Lindley, D. Dye, Evolution of lattice strain in Ti−6Al−4V during tensile loading at room temperature, Acta Mater. 56 (2008) 6186−6196, http://dx.doi.org/10.1016/j.actamat.2008.08.030.
[10] J.L.W. Warwick, J. Coakley, S.L. Raghunathan, R.J. Talling, D. Dye, Effect of texture on load partitioning in Ti-6Al-4V, Acta Mater. 60 (2012) 4117−4127, http://dx.doi.org/10.1016/j.actamat.2012.03.039.
[11] D. Gloaguen, G. Oum, V. Legrand, J. Fajoui, S. Branchu, Experimental and theoretical studies of intergranular strain in an alpha titanium alloy during plastic deformation, Acta Mater. 61 (2013) 5779−5790 (accessed 24.03.14), http://linkinghub.elsevier.com/retrieve/pii/S1359645413004540.
[12] D. Gloaguen, G. Oum, V. Legrand, J. Fajoui, M.-J. Moya, T. Pirling, et al., Intergranular strain evolution in titanium during tensile loading: neutron diffraction and polycrystalline model, Metall. Mater. Trans. A 46 (11) (2015) 5038−5046, http://dx.doi.org/10.1007/s11661-015-3073-3.
[13] J.L.W. Warwick, N.G. Jones, K.M. Rahman, D. Dye, Lattice strain evolution during tensile and compressive loading of CP Ti, Acta Mater. 60 (2012) 6720−6731.
[14] J.R. Cho, D. Dye, K.T. Conlon, M.R. Daymond, R.C. Reed, Intergranular strain accumulation in a near-alpha titanium alloy during plastic deformation, Acta Mater. 50 (2002) 4847−4864, http://dx.doi.org/10.1016/S1359-6454(02)00354-3.
[15] G. Martin, L. Naze, G. Cailletaud, Numerical multi-scale simulations of the mechanical behavior of β-metastable titanium alloys Ti5553 and Ti17, Procedia Eng. 10 (2011) 1803−1808, http://dx.doi.org/10.1016/j.proeng.2011.04.300.
[16] T. Duval, P. Villechaise, S. Andrieu, Mechanical properties and strain mechanisms analysis in Ti-5553 titanium alloy, Suppl. Proc. Gen. Pap. Sel. 3 (2011) 471−478.
[17] I.C. Noyan, J.B. Cohen, Residual Stress - Measurement by Diffraction and Interpretation, Springer-V, 1987.
[18] V. Hauk, Structural and Residual Stress Analysis by Nondestructive Methods, Elsevier, 1997.
[19] M. Herbig, 3D Short Fatigue Crack Investigation in Beta Titanium Alloys Using Phase and Diffraction Contrast Tomography, PhD Thesis, INSA de Lyon, 2011.
[20] J.C. Chesnutt, F.H. Froes, Effect of α-phase morphology and distribution on the tensile ductility of a metastable beta titanium alloy, Metall. Mater. Trans. A 8 (1977) 1013−1017.
[21] W. Kockelmann, L.C. Chapon, P.G. Radaelli, Neutron texture analysis on GEM at ISIS, Phys. B Condens. Matter 385 (2006) 639−643.
[22] A.C. Hannon, Results on disordered materials from the general materials diffractometer, GEM, at ISIS, Nucl. Instrum. Methods Phys. Res. Sect. A Accel. Spectrom. Detect. Assoc. Equip. 551 (2005) 88−107.
[23] B.L. Averbach, M. Cohen, X-ray determination of retained austenite by integrated intensities, Trans. AIME 176 (1948) 401−415.
[24] J. Durnin, K.A. Ridal, Determination of retained austenite in steel by X-ray diffraction, J. Iron Steel Inst. 206 (1968) 60−67.
[25] J.T. Bonarski, M. Wrobel, K. Pawlik, Quantitative phase analysis of duplex stainless steel using incomplete pole figures, Mater. Sci. Technol. 16 (2000) 657−662.
[26] V. Hounkpati, Analyse multiéchelle du comportement mécanique de matériaux métalliques biphasés, PhD Thesis, Ecole Centrale de Nantes, 2015.
[27] S. Shang, G. Hu, J. Shen, Determination of volume fraction in textured titanium alloy sheet, Scr. Mater. 45 (2001) 287−292, http://dx.doi.org/10.1016/S1359-6462(01)01028-4.
[28] J.R. Santisteban, M.R. Daymond, J.A. James, L. Edwards, ENGIN-X: a third-generation neutron strain scanner, J. Appl. Crystallogr. 39 (2006) 812−825, http://dx.doi.org/10.1107/S0021889806042245.
[29] C.M. Moreton-Smith, S.D. Johnston, F.A. Akeroyd, Open GENIE—a generic multi-platform program for the analysis of neutron scattering data, J. Neutron Res. 4 (1996) 41−47.
[30] V. Hounkpati, S. Fréour, D. Gloaguen, V. Legrand, Influence of morphologic texture on stress analysis by X-ray and neutron diffraction in single-phase metallic materials, J. Mater. Sci. 49 (2014) 7049−7065, http://dx.doi.org/10.1007/s10853-014-8410-1.
[31] E. Kröner, Zur plastischen verformung des vielkristalls, Acta Metall. 9 (1961) 155−161.
[32] R. Hill, Continuum micro-mechanics of elastoplastic polycrystals, J. Mech. Phys. Solids 13 (1965) 89−101.
[33] J.D. Eshelby, The determination of the elastic field of an ellipsoidal inclusion, and related problems, Proc. R. Soc. Lond. Ser. A. Math. Phys. Sci. 241 (1957) 376−396.
[34] D. Gloaguen, M. François, R. Guillén, J. Royer, Evolution of internal stresses in rolled Zr702 α, Acta Mater. 50 (2002) 871−880.
[35] D. Gloaguen, T. Berchi, E. Girard, R. Guillén, Measurement and prediction of residual stresses and crystallographic texture development in rolled Zircaloy-4 plates: X-ray diffraction and the self-consistent model, Acta Mater. 55 (2007) 4369−4379 (accessed 24.03.14), http://linkinghub.elsevier.com/retrieve/pii/S1359645407002443.
[36] J.W. Hutchinson, Elastic-plastic behaviour of polycrystalline metals and composites, Proc. R. Soc. Lond. A 319 (1970) 247−272.
[37] P. Lipinski, M. Berveiller, Elastoplasticity of micro-inhomogeneous metals at large strains, Int. J. Plast. 5 (1989) 149−172, http://dx.doi.org/10.1016/0749-6419(89)90027-2.
[38] R. Hill, The essential structure of constitutive laws for metal composites and polycrystals,, J. Mech. Phys. Solids 15 (1967) 79−95.
[39] P. Zattarin, A. Baczmański, P. Lipinski, K. Wierzbanowski, Modified self consistent model for time independent plasticity of polycrystalline material, Arch. Metall. 45 (2000) 163−184.
[40] G. Franz, F. Abed-Meraim, J.-P. Lorrain, T. Ben Zineb, X. Lemoine, M. Berveiller, Ellipticity loss analysis for tangent moduli deduced from a large strain elastic−plastic self-consistent model, Int. J. Plast. 25 (2009) 205−238, http://dx.doi.org/10.1016/j.ijplas.2008.02.006.
[41] J.-P. Lorrain, T. Ben Zineb, F. Abed-Meraim, M. Berveiller, Ductility loss modelling for BCC single crystals, Int. J. Form. Process 8 (2005) 135−158, http://dx.doi.org/10.3166/ijfp.8.135-158.
[42] D. Gloaguen, T. Berchi, E. Girard, R. Guillén, Prediction of intergranular strains using a modified self-consistent elastoplastic approach, Phys. Status Solidi A 203 (2006) R12−R14.
[43] F. Bridier, P. Villechaise, J. Mendez, Analysis of the different slip systems activated by tension in a α/β titanium alloy in relation with local crystallographic orientation, Acta Mater. 53 (2005) 555−567, http://dx.doi.org/10.1016/j.actamat.2004.09.040.
[44] T. Duval, Analyse multi-échelles des relations microstructure/propriétés mécaniques sous sollicitation monotone et cyclique des alliages de titane β-métastable, PhD Thesis, Ecole Nationale Supérieure de Mécanique et d'Aérotechnique, 2013.
[45] P. Franciosi, M. Berveiller, A. Zaoui, Latent hardening in copper and aluminium single crystals, Acta Metall. 28 (1980) 273−283.
[46] E.A. Brandes, G.B. Brook, Smithells Metals Reference Book, seventh ed., Butterwort, Oxford, 1992.
[47] G. Simmons, H. Wang, Single Crystal Elastic Constants and Calculated Aggregate Properties, The MIT Press, 1971.
[48] S. Fréour, D. Gloaguen, M. François, A. Perronnet, R. Guillén, Determination of single-crystal elasticity constants in a cubic phase within a multiphase alloy: X-ray diffraction measurements and inverse-scale transition modelling,

J. Appl. Crystallogr. 38 (2005) 30–37, http://dx.doi.org/10.1107/S0021889804023441.
[49] H. Ledbetter, H. Ogi, S. Kai, S. Kim, M. Hirao, Elastic constants of body-centered-cubic titanium monocrystals, J. Appl. Phys. 95 (2004) 4642–4644, http://dx.doi.org/10.1063/1.1688445.
[50] W. Petry, A. Heiming, J. Trampenau, M. Alba, C. Herzig, H.R. Schober, et al., Phonon dispersion of the bcc phase of group-IV metals. I. bcc titanium, Phys. Rev. B 43 (1991) 10933–10947, http://dx.doi.org/10.1103/PhysRevB.43.10933.
[51] B. Clausen, T. Lorentzen, M. Bourke, M.R. Daymond, Lattice strain evolution during uniaxial tensile loading of stainless steel, Mater. Sci. Eng. A 259 (1999) 17–24. http://linkinghub.elsevier.com/retrieve/pii/S0921509398008788.
[52] F. Xu, R. a. Holt, M.R. Daymond, Modeling lattice strain evolution during uniaxial deformation of textured Zircaloy-2, Acta Mater. 56 (2008) 3672–3687, http://dx.doi.org/10.1016/j.actamat.2008.04.019.
[53] C.J. Neil, J. a. Wollmershauser, B. Clausen, C.N. Tomé, S.R. Agnew, Modeling lattice strain evolution at finite strains and experimental verification for copper and stainless steel using in situ neutron diffraction, Int. J. Plast. 26 (2010) 1772–1791, http://dx.doi.org/10.1016/j.ijplas.2010.03.005.
[54] O. Muránsky, D.G. Carr, M.R. Barnett, E.C. Olivier, P. Sittner, Investigation of deformation mechanisms involved in the plasticity of AZ31 Mg alloy: in situ neutron diffraction and EPSC modelling, Mater. Sci. Eng. A 496 (2008) 14–24 (accessed 22.03.14), http://linkinghub.elsevier.com/retrieve/pii/S092150930800823X.